

Remeshing-Free Graph-Based Finite Element Method for Ductile and Brittle Fracture

AVIRUP MANDAL, Indian Institute of Technology Bombay, India

PARAG CHAUDHURI, Indian Institute of Technology Bombay, India

SUBHASIS CHAUDHURI, Indian Institute of Technology Bombay, India

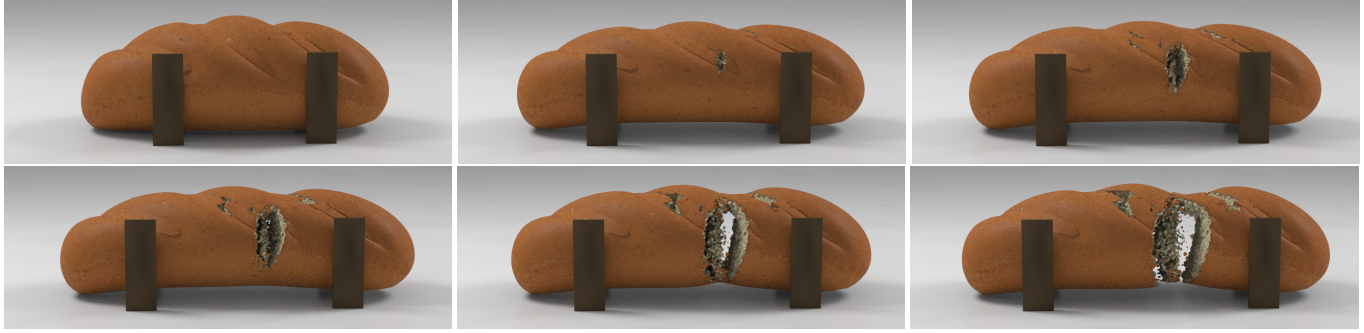


Fig. 1. Our model produces the intricate fracture patterns that result from the tearing of a loaf of bread. We show rendered frames from the simulation (to be seen left to right, top to bottom). The loaf model has around 620k tetrahedra.

This paper presents a remeshing-free, graph-based finite element method (FEM) for simulating ductile and brittle fracture. Since fracture produces new mesh fragments and introduces additional degrees of freedom in the system dynamics, existing FEM based methods suffer from an explosion in computational cost as the system matrix size increases. Our model develops an algorithm for modelling fracture on the graph induced in a volumetric mesh with tetrahedral elements, by its vertices and edges. In order to initialize and propagate fracture, We simply relabel the edges of the graph using a damage variable, and control the diffusion of fracture inside the object by varying the support of a damage kernel. We present the reformulated system dynamics for this relabeled graph that allows us to simulate fracture in a FEM setting, without changing the size of system dynamics matrix of the mesh. This makes our computational method remeshing-free and scalable to high-resolution meshes. The fracture surface has to be reconstructed explicitly for visualization purposes only. We evaluate our algorithm extensively on a variety of brittle and ductile materials and compare its features with other state of the art methods. We simulate standard laboratory experiments from structural mechanics and compare the results visually and quantitatively with real-world experiments performed on physical material samples. We also present results evaluating the performance of our method, and show that our techniques offer stability and speed that is unmatched in current literature.

CCS Concepts: • **Computing methodologies** → **Physical simulation**; • **Theory of computation** → **Network flows**.

Additional Key Words and Phrases: fracture, remeshing-free, FEM, graph-based

Authors' addresses: Avirup Mandal, avirupmandal@ee.iitb.ac.in, Indian Institute of Technology Bombay, Powai, Mumbai, Maharashtra, India, 400076; Parag Chaudhuri, parag@cse.iitb.ac.in, Indian Institute of Technology Bombay, Powai, Mumbai, Maharashtra, India, 400076; Subhasis Chaudhuri, sc@ee.iitb.ac.in, Indian Institute of Technology Bombay, Powai, Mumbai, Maharashtra, India, 400076.

1 INTRODUCTION

Fracture of objects is an ubiquitous phenomena in the real world. Everyday we come across several instances of fracture, ranging from shattering of brittle glass tumbler to tearing of a soft loaf of bread. In order to recreate such real world phenomena, realistic dynamic fracture simulations are used frequently in computer graphics. Simulating intricate fracture patterns and crack propagation often requires complex mathematical formulation. It has thus been an important research topic in both structural mechanics and computer graphics. Incorporating both brittle and ductile fracture in a single framework needs even more sophisticated analysis.

However, despite intensive research for last two decades, the existing fracture techniques still suffer from scalability issues, poor stability and high computational cost. E.g., as the number of cracks grow in an object, the Finite Element Method (FEM) based approaches proposed in [O'Brien et al. 2002] and [O'Brien and Hodgins 1999] require remeshing to address the additional degrees of freedom (DOF). This poses challenges like generation of thin (or sliver) elements, instability and heavy computational cost. To avoid these effects authors have explored remeshing-free techniques like eXtended Finite Element Method (XFEM) [Koschier et al. 2017] [Chitalu et al. 2020] and the Material Point Method (MPM) [Pauly et al. 2005] [Wang et al. 2019] [Hu et al. 2018a] [Wolper et al. 2019] [Wolper et al. 2020]. The system matrix of XFEM scales rapidly with the introduction of cracks. Each new crack introduces new DOF, which in turn leads to severe stability issues. On the other hand, the particle based material point methods have shortcomings with respect to imposing boundary conditions, high computational cost and rigidity of fragmented segments. Contrary to the discrete formulations, peridynamics based methods [Chen et al. 2018] [Levine et al. 2015] and boundary element methods (BEM) [Hahn and Wojtan 2015] [Hahn

and Wojtan 2016] deal with solving the integral equations of continuum mechanics, thus bypassing the difficulty of imposing boundary conditions. But solving these singular integrals is extremely expensive and therefore, is not suitable for low resource applications.

We perform our simulations on volumetric meshes with tetrahedral elements. This underlying mesh, on which all computation is performed, is called the computational mesh. This mesh induces a graph where its vertices become the nodes of the graph and the edges of the mesh become the edges of the graph. The computational mesh is never remeshed. This implies that unlike XFEM, the number of degrees of freedom of the system does not change with the introduction of cracks, i.e., the size of initial system matrix does not change. This allows our method to scale to high resolution models with very little extra computational overhead. The mesh that is rendered for visualization is the same as the computational mesh initially. This mesh however, needs to be split and the fracture surfaces have to be reconstructed for rendering the fracture. This does not affect the computational mesh.

It has been shown in earlier work that the nodal forces of a discretized hyper-elastic FEM system can be completely represented in terms of a function of strain energy density along the edges of the induced graph [Reddy and Srinivasa 2015]. We use this fact and follow prior work in structural mechanics [Khodabakhshi et al. 2016] to define a purely edge based damage variable, which describes the extent of damage for any edge in the graph. We build over prior work to reformulate the strain energy of damaged elements in 3D volumetric object meshes and then simulate independent movement of the fractured pieces. Further in our model, we can generate and control the diffusion of cracks into the object by imposing a non-local fracture criteria.

We demonstrate the efficacy and robustness of our method by simulating realistic examples of both brittle and ductile fracture. Our method’s ability to handle fracture of a variety of materials ranging from stiff glass to squishy jello makes it useful for wide range of applications.

Our contributions are summarized as follows:

- We propose a novel remeshing-free, graph-based, computationally efficient and robust FEM solution for fracture simulation of 3D models.
- We generalize our graph-based FEM algorithm to simulate fracture of materials with both linear and non-linear strain energy.
- We demonstrate how our method serves as a unified FEM framework to simulate both brittle and ductile fracture.

The rest of the paper is organized as follows. We start by presenting a discussion of related works in Section 2. Subsequently, in Section 3 we first describe the formulation of graph-based FEM, and then detail the technical aspects of fracture via crack initiation and crack propagation. We briefly discuss the visualization of fractured material in Section 4. Next, we present results for various kinds of materials undergoing fracture, generated using our method in Section 5. In order to validate our method and check its correctness, we compare our results with real world benchmark fracture experiments and existing fracture simulation techniques in literature.

Finally, we conclude our paper by discussing the limitations of our work and future work.

2 RELATED WORK

We first delve into existing methods for mesh based fracture simulation in computer graphics. Next, we explore meshless particle based fracture simulation methods. We conclude the section by reviewing graph-based finite element analysis presented in material science literature.

2.1 Mesh-based Fracture Simulation

The inception of fracture simulation in computer graphics goes back to the seminal work on visco-elastic fracture by Terzopoulos et al. [Terzopoulos and Fleischer 1988]. Early approaches propose to model brittle fracture by removing the springs in a mass-spring system [Aoki et al. 2004] [Norton et al. 1991] [Hirota et al. 2000] [Hirota et al. 1998] depending on a stress-based yield threshold. But in such a system, where point masses are connected by springs, sudden removal of springs leads to significant visual artifacts. Moreover, visualization of the crack surface often requires the use of a tetrahedral marching algorithm and is therefore computationally expensive [Hirota et al. 2000] [Hirota et al. 1998]. Later, finite element method based solutions for simulating fracture have been more successful and different variations of those approaches are still widely used. The first breakthrough in FEM based fracture came in the paper by O’Brien and Hodgins [O’Brien and Hodgins 1999]. In their work, the authors present a nodal stress-based analysis for brittle fracture that was later extended further to ductile fracture [O’Brien et al. 2002] [Müller and Gross 2004]. Bao et al. [Bao et al. 2007] also present a method to simulate both brittle and ductile fracture. These FEM based fracture techniques rely on splitting the elements of a tetrahedral mesh, which satisfy the fracture conditions and then remesh the entire fractured mesh with the crack opening. However, these approaches pose various geometric difficulties like remeshing near crack tips, generation of degenerate elements, forming ill-conditioned basis matrices. Subsequent FEM based approaches employ different techniques to alleviate these problems, as such, dynamic local mesh refinement to repair degenerate tetrahedra [Wicke et al. 2010], remeshing depending on gradient descent flow for finer fracture resolution [Chen et al. 2014], adaptive subdivision schemes for tetrahedral [Koschier et al. 2015] and triangular meshes [Pfaff et al. 2014] where remeshing is done around the high stress areas to improve fracture resolution.

FEM based solutions that work with a virtual node algorithm (VNA) [Molino et al. 2004] duplicate elements and add extra degrees of freedom to facilitate partial or full crack openings, instead of splitting the mesh elements. Later, VNA based methods are improved to incorporate cutting at lower than mesh resolution [Sifakis et al. 2007] and to robustly handle intersections passing through node, edge or face through an adaptive element duplication approach [Wang et al. 2015]. Recently, Koschier et al. [Koschier et al. 2017] presented a remeshing-free extended finite element method (XFEM) based algorithm to simulate the dynamic pre-defined cuts in a 3D mesh. Like VNA, XFEM too adds extra degrees of freedom using enrichment functions but the advantage of XFEM over VNA

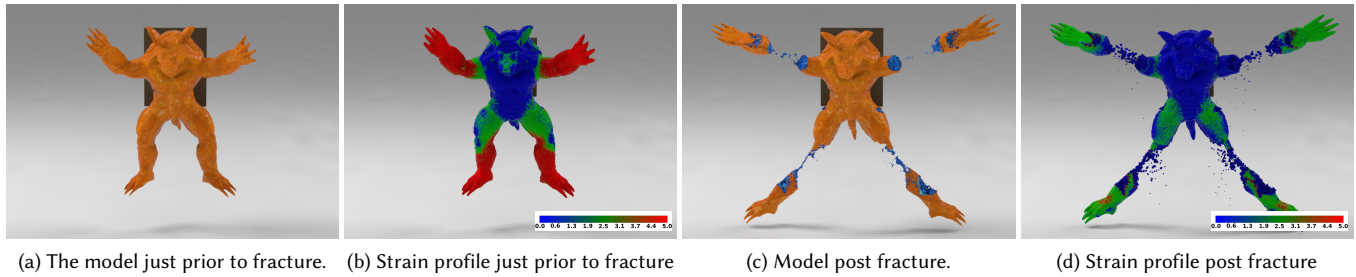


Fig. 2. Here we show frames from a simulation where we rip off the limbs of a jello armadillo. In the strain profiles, red to blue colour gradient denotes highest to lowest strain values. The model fractures where the strain is highest prior to fracture. Post fracture, the strain drops.

is while VNA duplicates the mesh element leading to an erratic conservation of mass, XFEM splits the initial mass of an element into fragments. Chitalu et al. [Chitalu et al. 2020] expanded the pre-defined cuts to crack generation and propagation, and also incorporated crack-tip enrichment for simulating partially fractured tetrahedra.

Contrary to processing fracture in volume elements like FEM, boundary element methods (BEM) simulate cracks on a surface mesh. Even though BEM found its way into graphics by James et al. [James and Pai 1999] for simulating elastostatic deformable objects, it has been used recently for fracture simulation. Hahn et al. [Hahn and Wojtan 2015] and Zhu et al. [Zhu et al. 2015] used BEM with stress intensity factors (SIFs) along crack fronts to successfully simulate brittle fracture. Later Hahn et al. [Hahn and Wojtan 2016] expanded their work to develop an algorithm for fast approximation of BEM brittle fracture, alleviating the high computational cost for solving singular integrals. Currently there exists no work on BEM ductile fracture.

Peridynamics methods solve the integral equations of continuum mechanics. Unlike discrete differential-based methods, e.g. FEM or MPM, which need to impose necessary boundary conditions for simulating fracture, it is trivial to model discontinuities using integral-based peridynamics. In initial work using these ideas, authors [Levine et al. 2015] approximate the behaviour of peridynamics using mass-spring systems to simulate brittle fracture. Later work [Chen et al. 2018] presents original peridynamics based fracture algorithms to simulate brittle as well as ductile fracture.

2.2 Meshless Fracture Simulation

Among the meshless methods, material point methods have gained considerable recognition in recent years. First major breakthrough of MPM in computer graphics came through the seminal work in snow simulation by Stomakhin et al. [Stomakhin et al. 2013]. Later MPM has found its application in simulating a wide range of materials as such chocolate, lava, hybrid fluids and rubber to name a few. Interested readers can look at [Jiang et al. 2016] for a detailed overview of different MPM methods. Most recently, MPM has shown promising results in simulating fracture due to its ability to handle extreme topological change. Hu et al. [Hu et al. 2018a] propose the Compatible Particle-in-Cell (CPIC) algorithm, which allows the simulation of sharp discontinuities inside a material and thus simulates

dynamic material cutting. Later Wolper et al. [Wolper et al. 2019], introduce Continuum Damage Mechanics (CDM) with a variational energy-based formulation for crack evolution. This achieves a realistic dynamic fracture simulation for isotropic materials. Further study [Wolper et al. 2020] devoted to formulating non-local CDM to simulate anisotropic material fracture.

MPM methods reproduce realistic fracture phenomena but they are not well suited to rendering sharp boundaries. They not only have difficulty in enforcing essential boundary conditions, they also suffer from disappearance of intricate crack patterns due to excessive smoothing, high computational cost and rigidity of fragmented elements. Further, MPM methods struggle to simulate rigid object fracture.

2.3 Graph-based Finite Element Method

While simulating fractures in the material domain, classical FEM introduces degenerate elements due to remeshing and XFEM has severe limitations to incorporating a large number of cracks due to rapid scaling up of the system matrix. Moreover, both of them suffer from stability issues and high computational cost. While BEM and peridynamics overcome these problems by solving direct integrals, they demand prohibitively high numerical computation. Again, use of BEM is limited to materials with large volumes. Meshless methods have their own limitations as described above.

Work in finite element analysis literature by Reddy et al. [Reddy and Srinivasa 2015] proposes a solution based on classical FEM to show that for any hyper-elasticity problem, the magnitude of the nodal forces can be written completely in terms of strain energy density along the edges composing the elements, while force directions are along the unit vectors corresponding to the edges. Using this idea in subsequent work, authors [Khodabakhshi et al. 2016] introduce Graph-based Finite Element Analysis (Gra-FEA) where a damage variable corresponding to the edges of composing elements is used. It is based on the strain threshold and thus can simulate the fracture of an object by weakening the material. The advantage of using Gra-FEA is that it requires no remeshing, while adding little computational overhead on FEM and it still retains all the advantages of FEM. The dependency of Gra-FEA on the underlying mesh structure is thoroughly studied in another work [Khodabakhshi et al. 2019]. Our work introduces Gra-FEA to the visual simulation of fracture for computer graphics. Existing literature referred above

on Gra-FEA only focuses on 2D materials consisting of triangular elements with linear strain energy. We extend the idea to 3D domain and our fracture algorithm can handle linear as well as non-linear strain energy. The original Gra-FEA formulation is restricted to simulating fracture for brittle materials. Our algorithm is capable of simulating fracture for both brittle and ductile materials. We believe, to the best of our knowledge, that this is the first work in computer graphics to simulate fracture of 3D brittle, as well as ductile objects, with linear or non-linear strain energy using the graph-based FEM.

3 GOVERNING METHODS

We briefly derive the formulation of graph-based FEM from the theory of classical FEM. Then we delve into the details of fracture generation using graph-based FEM. In our work, we always use tetrahedral finite elements with a linear basis for domain discretization.

3.1 Classical FEM

Consider a three-dimensional domain $\Omega \in \mathbb{R}^3$ that is discretized into a mesh of n_{tet} tetrahedra. Moreover, let \mathfrak{V} be the set of nodes n_v shared by the tetrahedral mesh elements Δ_e . As shown in Figure 3, a displacement function, $\mathbf{u} : \Omega \times [0, \infty) \rightarrow \mathbb{R}^3$, can be defined as a mapping from a material point $\xi \in \Omega$ to its deformed location $\mathbf{x} \in \Omega_t$ in the world space. Ω_t represents the world space at time t . At a certain timestep $t \in [0, \infty)$, the displacement function can be represented as

$$\mathbf{u}(\xi, t) = \sum_{i \in \mathfrak{V}} \mathbf{N}_i(\xi) \mathbf{u}_i(t), \quad (1)$$

where $\mathbf{N}_i(\xi)$ is the shape function and \mathbf{u}_i is the displacement vector at the node i . For the sake of brevity of notation, we drop the shape (ξ) and time (t) parameters for the shape and displacement functions in further discussion.

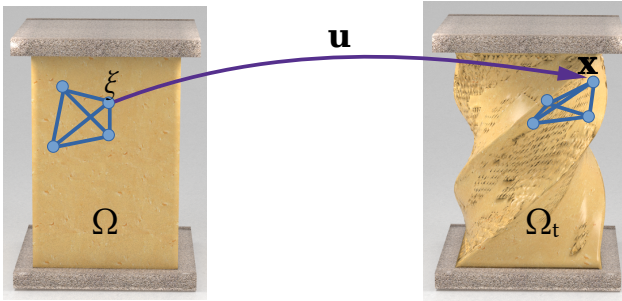


Fig. 3. Deformable object: A displacement function maps a point on the object in material coordinates on the left and to world coordinates on the right.

The core idea of deformable object simulation is that when an object mesh is deformed from its rest position, a hyper-elastic strain energy Ψ , develops inside it. The strain energy produces internal elastic force \mathbf{f}^{int} , which in turn tries to restore the rest shape of the mesh. Thus, the system dynamics of deformed object can be written

in Lagrange's form as

$$\mathbf{M}\ddot{\bar{\mathbf{u}}} + \mathbf{B}\dot{\bar{\mathbf{u}}} + \mathbf{f}^{int} = \mathbf{f}^{ext} \quad (2)$$

$$\bar{\mathbf{u}} = (\mathbf{u}_1^T \dots \mathbf{u}_{n_v}^T)^T \quad (3)$$

Here \mathbf{M} and \mathbf{B} are the mass and damping matrices of full system. \mathbf{f}^{ext} and \mathbf{f}^{int} represent the external force vector and internal force vector respectively. Now Equation 2 can further be simplified as the sum of parameters from each individual tetrahedral element.

$$\sum_{e=1}^{n_{tet}} \mathbf{m}_e \ddot{\bar{\mathbf{u}}} + \sum_{e=1}^{n_{tet}} \mathbf{b}_e \dot{\bar{\mathbf{u}}} + \sum_{e=1}^{n_{tet}} \mathbf{f}_e^{int} = \sum_{e=1}^{n_{tet}} \mathbf{f}_e^{ext} \quad (4)$$

$$\mathbf{m}_e = \int_{\Delta_e} \rho_0 \mathbf{N}_e^T \mathbf{N}_e d\xi \quad (5)$$

$$\mathbf{f}_e^{ext} = \int_{\Delta_e} \mathbf{N}_e^T \mathbf{t}_e d\xi \quad (6)$$

$$\mathbf{f}_e^{int} = \int_{\Delta_e} \mathbf{s}_e(\bar{\mathbf{u}}, \xi) d\xi \quad (7)$$

$$\mathbf{N}_e = [\mathbf{N}_0 \mathbf{I}_3 \ \mathbf{N}_1 \mathbf{I}_3 \ \mathbf{N}_2 \mathbf{I}_3 \ \mathbf{N}_3 \mathbf{I}_3]. \quad (8)$$

While \mathbf{m}_e is the mass matrix of a tetrahedral element, \mathbf{N}_e , \mathbf{t}_e , \mathbf{f}_e^{ext} and \mathbf{f}_e^{int} represent element shape function vector, reference body force, external element force vector and internal element force vector respectively. \mathbf{I}_3 refers to 3×3 identity matrix.

Specific elastic element force, \mathbf{s}_e , is defined as

$$\mathbf{s}_e = \frac{\partial \Psi^e}{\partial \mathbf{u}} \quad (9)$$

where Ψ^e is elemental hyper-elastic strain energy.

$\mathbf{b}_e = \alpha \mathbf{m}_e + \beta \mathbf{k}_e + \tilde{\mathbf{b}}_e$ is the per element control damping matrix. Scalar quantities α and β control the level of 'mass' and 'stiffness' damping respectively while $\tilde{\mathbf{b}}_e$ is a user defined additional damping matrix.

The gradient of \mathbf{f}_e^{int} with respect to \mathbf{u} is called tangent stiffness matrix \mathbf{k}_e .

$$\mathbf{k}_e = \int_{\Delta_e} \frac{\partial \mathbf{f}_e^{int}}{\partial \mathbf{u}} d\xi \quad (10)$$

The stiffness matrix of full system, \mathbf{K} , can be represented as

$$\mathbf{K} = \sum_{e=1}^{n_{tet}} \mathbf{k}_e \quad (11)$$

Interested readers can look into the review paper by Sifakis and Barbic [Sifakis and Barbic 2012] for further details. In this work, we developed our fracture simulation model based on works by Smith et al. [Smith et al. 2018], Sin et al. [Sin et al. 2013] and Bargteil et al. [Bargteil et al. 2007]. Table 1 summarizes some of the quantities that we use frequently in FEM simulations.

Symbol	Definition
$\mathbf{F} = \mathbf{I} + \nabla_{\xi} \mathbf{u}$	Deformation gradient
$J = \det(\mathbf{F})$	Relative volume change
$\mathbf{C} = \mathbf{F}^T \mathbf{F}$	Right Cauchy-Green deformation tensor
$I_C = \text{trace}(\mathbf{C})$	First Right Cauchy-Green invariant
$II_C = \text{trace}(\mathbf{C}^2)$	Second Right Cauchy-Green invariant
$III_C = \det(\mathbf{C})$	Third Right Cauchy-Green invariant
$\mathbf{E} = \frac{1}{2} (\mathbf{F}^T \mathbf{F} - \mathbf{I})$	Lagrangian finite strain tensor
$\mathbf{P}(\mathbf{F}) = \frac{\partial \Psi}{\partial \mathbf{F}}$	First Piola-Kirchhoff stress tensor

Table 1. Quantities frequently used in FEM

3.2 Graph-based FEM

Let the hyper-elastic strain energy of a tetrahedral element, Δ_e , be Ψ^e and $\mathbf{f}_{e_i}^{int}$ be the internal elastic force acting on the i^{th} node of the element. Now it can be proved [Reddy and Srinivasa 2015] that nodal internal elastic forces of Δ_e can always be decomposed along the vectors connecting the nodes of Δ_e . The statement can be mathematically formulated as

$$\mathbf{f}_{e_i}^{int} = -V_e \frac{\partial \Psi^e}{\partial \mathbf{r}_i^e} = 2V_e \sum_{\substack{j=1 \\ j \neq i}}^{n_e} \frac{\partial \Psi^e}{\partial (d_{ij}^e)^2} d_{ij}^e \hat{\mathbf{d}}_{ij}^e \quad (12)$$

where $d_{ij}^e = \|\mathbf{r}_i^e - \mathbf{r}_j^e\|$ is the distance between the i^{th} and j^{th} nodes of Δ_e and $\hat{\mathbf{d}}_{ij}^e$ is unit vector along d_{ij}^e . Moreover, V_e and n_e represent volume and the number of nodes of Δ_e respectively. It can be seen from Equation 12 that the magnitude of the nodal internal elastic forces depend only on strain energy density of the element while the force directions are along its edges.

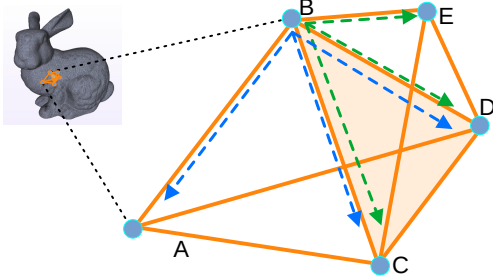


Fig. 4. Nodal force distribution along the edges for graph-based FEM.

Figure 4 shows two tetrahedral elements, Δ_eABDC and Δ_eBEDC , which share a common face. These can be thought of as being a part of a larger object mesh. We assume that the overall mesh is deformed and each node in the mesh develops internal elastic force. Now according to Equation 12, internal elastic force on the node B for Δ_eABDC can be written along the edges of Δ_eABDC as $\mathbf{f}_{\Delta_eABDC}^B = \mathbf{f}_{\Delta_eABDC}^{BC} + \mathbf{f}_{\Delta_eABDC}^{BA} + \mathbf{f}_{\Delta_eABDC}^{BD}$ (shown as dotted blue lines). Similarly, internal elastic force on the node B for Δ_eBEDC can be written along the edges of Δ_eBEDC as $\mathbf{f}_{\Delta_eBEDC}^B = \mathbf{f}_{\Delta_eBEDC}^{BC} + \mathbf{f}_{\Delta_eBEDC}^{BD} + \mathbf{f}_{\Delta_eBEDC}^{BE}$

(shown as dotted green lines). The distribution of nodal internal elastic forces for the entire mesh can be computed similarly.

3.3 Fracture with Graph-based FEM

In this section, we present our model for edge based fracture derived from Graph-based FEM. We take advantage of the fact that stress of an element is always a function of hyper-elastic strain energy density. We can find normal stress in the direction of the edges of a tetrahedral element by using a suitable transformation. Next, depending on the state of edge i.e., broken or unbroken, we manipulate the normal stress along the edges to degrade the strain energy density for a damaged element. Finally, using this updated strain energy density, we recalculate the elastic forces and tangent stiffness matrix for fracture simulation.

Using chain rule of differentiation and deformation gradient from Table 1, we can rewrite the Equation 12 as

$$\mathbf{f}_{e_i}^{int} = 2V_e \sum_{\substack{j=1 \\ j \neq i}}^{n_e} \sum_{k=1}^3 \sum_{l=1}^3 \left[\frac{\partial \Psi^e}{\partial [\mathbf{F}]_{kl}} \frac{\partial [\mathbf{F}]_{kl}}{\partial (d_{ij}^e)^2} \right] d_{ij}^e \hat{\mathbf{d}}_{ij}^e \quad (13)$$

where $\frac{\partial \Psi^e}{\partial [\mathbf{F}]_{kl}}$ are components of first Piola-Kirchhoff stress tensor of Δ_e (see Table 1). Thus, the edge based elastic forces can be completely represented as a function of stress in Δ_e . This stress in turn depends on the derivative of element strain energy, Ψ^e w.r.t. the deformation gradient \mathbf{F} . Therefore, by manipulating the stress components properly we can change the internal elastic forces and in turn simulate fracture of an element.

Let the rectangular Cartesian components of the Piola-Kirchhoff stress tensor, σ_c^e , be denoted as

$$\sigma_c^e = \begin{bmatrix} \sigma_{xx}^e & \sigma_{yy}^e & \sigma_{zz}^e & \sigma_{xy}^e & \sigma_{xz}^e & \sigma_{yz}^e \end{bmatrix} \quad (14)$$

The set of normal stress along the edges is represented as

$$\sigma_f^e = \begin{bmatrix} \sigma_{12}^e & \sigma_{13}^e & \sigma_{14}^e & \sigma_{23}^e & \sigma_{24}^e & \sigma_{34}^e \end{bmatrix} \quad (15)$$

where σ_{mn}^e represents the normal stress along the edge formed by nodes m and n in Equation 15. Then the transformation of Cartesian stress to normal stress in the direction of an edge can be formulated as below [Reddy and Srinivasa 2015][Khodabakhshi et al. 2016]

$$\begin{aligned} \sigma_{mn}^e &= \sigma_{xx}^e \cos^2 \phi_x + \sigma_{yy}^e \cos^2 \phi_y + \sigma_{zz}^e \cos^2 \phi_z \\ &+ \sigma_{xy}^e \cos \phi_x \cos \phi_y + \sigma_{xz}^e \cos \phi_x \cos \phi_z + \sigma_{yz}^e \cos \phi_y \cos \phi_z \end{aligned} \quad (16)$$

Assuming that $\hat{\mathbf{d}}_{mn}^e$, $\hat{\mathbf{x}}$, $\hat{\mathbf{y}}$ and $\hat{\mathbf{z}}$ denote unit vectors along the edge formed by nodes m and n of the tetrahedral element Δ_e , x -axis, y -axis and z -axis respectively, the following relations hold true

$$\cos \phi_x = \hat{\mathbf{d}}_{mn}^e \cdot \hat{\mathbf{x}}, \quad \cos \phi_y = \hat{\mathbf{d}}_{mn}^e \cdot \hat{\mathbf{y}}, \quad \cos \phi_z = \hat{\mathbf{d}}_{mn}^e \cdot \hat{\mathbf{z}}, \quad (17)$$

Using Equation 16, we can write the final relation between two sets of strains as:

$$[\sigma_{12}^e \quad \sigma_{13}^e \quad \sigma_{14}^e \quad \sigma_{23}^e \quad \sigma_{24}^e \quad \sigma_{34}^e]^T = \mathbf{T} \begin{bmatrix} \sigma_{xx}^e \\ \sigma_{yy}^e \\ \sigma_{zz}^e \\ \sigma_{xy}^e \\ \sigma_{xz}^e \\ \sigma_{yz}^e \end{bmatrix} \quad (18)$$

where, for convenience of notation, if we denote $\cos \phi$ as $c\phi$, then

$$\mathbf{T} = \begin{bmatrix} c^2\phi_x^{12} & c^2\phi_y^{12} & c^2\phi_z^{12} & c\phi_x^{12}c\phi_y^{12} & c\phi_x^{12}c\phi_z^{12} & c\phi_y^{12}c\phi_z^{12} \\ c^2\phi_x^{13} & c^2\phi_y^{13} & c^2\phi_z^{13} & c\phi_x^{13}c\phi_y^{13} & c\phi_x^{13}c\phi_z^{13} & c\phi_y^{13}c\phi_z^{13} \\ c^2\phi_x^{14} & c^2\phi_y^{14} & c^2\phi_z^{14} & c\phi_x^{14}c\phi_y^{14} & c\phi_x^{14}c\phi_z^{14} & c\phi_y^{14}c\phi_z^{14} \\ c^2\phi_x^{23} & c^2\phi_y^{23} & c^2\phi_z^{23} & c\phi_x^{23}c\phi_y^{23} & c\phi_x^{23}c\phi_z^{23} & c\phi_y^{23}c\phi_z^{23} \\ c^2\phi_x^{24} & c^2\phi_y^{24} & c^2\phi_z^{24} & c\phi_x^{24}c\phi_y^{24} & c\phi_x^{24}c\phi_z^{24} & c\phi_y^{24}c\phi_z^{24} \\ c^2\phi_x^{34} & c^2\phi_y^{34} & c^2\phi_z^{34} & c\phi_x^{34}c\phi_y^{34} & c\phi_x^{34}c\phi_z^{34} & c\phi_y^{34}c\phi_z^{34} \end{bmatrix} \quad (19)$$

The criteria for fracture in graph-based FEM is that if the weighted average of normal stress along the direction of any edge exceeds the critical stress threshold σ_{thres}^e , a crack is to be formed on that edge. Using Equations 14 and 18 the fracture criteria can, therefore, be defined as

$$\sigma_{mn}^{e*} = \left[\mathbf{T} \left(\sum_{\|\mathbf{r}-\mathbf{r}_0\| \leq R_d} \omega(\mathbf{r}-\mathbf{r}_0) \sigma_c^e(\mathbf{r}) \right) \right]_{mn} \geq \sigma_{thres}^e \quad (20)$$

where σ_{mn}^{e*} is a component of weighted average of normal stress along the edge formed by nodes m and n , ω is a weight kernel and R_d is support of the kernel. While vector \mathbf{r} refers to position of centroid of any tetrahedron in the mesh, \mathbf{r}_0 denotes the position of centroid of the reference tetrahedron. As the support of kernel, R_d , increases, the cracks become more diffused i.e., they spread more inside the object [Khodabakhshi et al. 2019]. For $R_d = 0$, the fracture criteria depends only on the reference tetrahedron, resembling a local fracture. Now for each edge of the mesh, we

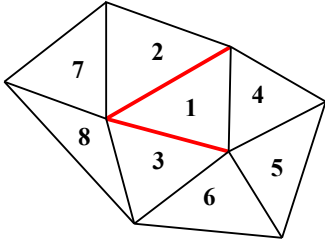


Fig. 5. Fractured edges shared multiple elements.

maintain a binary damage variable, $\zeta \in \{0, 1\}$. A value of $\zeta = 0$ corresponds to unbroken edge, while $\zeta = 1$ implies crack is formed on the edge.

$$\zeta = \begin{cases} 0 & \text{if } \sigma_{mn}^{e*} < \sigma_{thres} \\ 1 & \text{if } \sigma_{mn}^{e*} \geq \sigma_{thres} \end{cases} \quad (21)$$

As evident from Equation 20, the number of broken edges in a tetrahedral element may vary from zero to six. Once an edge is broken, it will not get repaired in subsequent iterations and all the

tetrahedra that share the broken edge will be considered damaged. As an example, a shared edge fracture is depicted in Figure 5, using a simplified, two-dimensional example. Two edges in the mesh, colored red, are broken. These broken edges are shared by triangles 1 (two edges), 2 (one edge) and 3 (one edge). In the subsequent iterations, all three triangular elements will be considered damaged with varying degrees of damage. Whenever an edge, e_{br} , gets broken, the corresponding normal stress of that edge becomes zero for all elements sharing that edge. Using Equations 18 and 21, we can write

$$\begin{bmatrix} \sigma_{12}^{e'} \\ \sigma_{13}^{e'} \\ \sigma_{14}^{e'} \\ \sigma_{23}^{e'} \\ \sigma_{24}^{e'} \\ \sigma_{34}^{e'} \end{bmatrix} = \begin{bmatrix} \zeta_{12} & 0 & 0 & 0 & 0 & 0 \\ 0 & \zeta_{13} & 0 & 0 & 0 & 0 \\ 0 & 0 & \zeta_{14} & 0 & 0 & 0 \\ 0 & 0 & 0 & \zeta_{23} & 0 & 0 \\ 0 & 0 & 0 & 0 & \zeta_{24} & 0 \\ 0 & 0 & 0 & 0 & 0 & \zeta_{34} \end{bmatrix} \begin{bmatrix} \sigma_{12}^e \\ \sigma_{13}^e \\ \sigma_{14}^e \\ \sigma_{23}^e \\ \sigma_{24}^e \\ \sigma_{34}^e \end{bmatrix} \quad \forall e_{br} \in \Delta_e \quad (22)$$

where ζ_{mn} and $\sigma_{mn}^{e'}$ are damage variable and stress after fracture along the edge formed by nodes m and n .

3.4 Hyper-elastic Strain Energy for Fracture

We update system equation of fractured mesh using a linear reformulation of elastic energy. In contrast, the work of Gra-FEA [Khodabakhshi et al. 2016] defines the updated elastic energy as a function of edge based stress $\sigma_{mn}^{e'}$ such as $\Psi_{new}^e = f(\sigma_{12}^{e'}, \sigma_{13}^{e'}, \sigma_{14}^{e'}, \sigma_{23}^{e'}, \sigma_{24}^{e'}, \sigma_{34}^{e'})$. However, it only considers linear elasticity and 2D models in their work. For non-linear elasticity and 3D models, doing this kind of update is non-trivial and computationally expensive.

Our linear reformulation of elastic energy makes it amenable for visual simulation and works for non-linear elasticity and 3D models, at the cost of adding a little error due to the linearization.

Using Equation 22 the new elastic energy for fractured elements is defined as

$$\begin{aligned} \Psi_{new}^e &= \left(\frac{|\sigma_{12}^{e'}| + |\sigma_{13}^{e'}| + |\sigma_{14}^{e'}| + |\sigma_{23}^{e'}| + |\sigma_{24}^{e'}| + |\sigma_{34}^{e'}|}{|\sigma_{12}^e| + |\sigma_{13}^e| + |\sigma_{14}^e| + |\sigma_{23}^e| + |\sigma_{24}^e| + |\sigma_{34}^e|} \right) \Psi^e \\ &= \chi^e \Psi^e \end{aligned} \quad (23)$$

where χ^e signifies the fractured elastic strain energy as fraction of original one depending on the number of damaged edges. It is important to note here that when an element fractures into two or more disjoint fragments, we assign zero value to the fractured elastic strain energy i.e. $\Psi_{new}^e = 0$, in Equation 23.

3.5 Updated System Equations

Using the new elastic strain energy density from Equation 23, we rewrite the FEM system dynamics of the mesh to incorporate fracture. Following the arguments presented in [Xu et al. 2015] the parameters of the system dynamics of fractured object are updated as below.

Internal elastic force, using Equations 7 and 9,

$$\begin{aligned} \mathbf{f}_e^{int*} &= \chi^e \int_{\Delta_e} \frac{\partial \Psi^e}{\partial \mathbf{u}} d\xi = \chi^e \int_{\Delta_e} \left(\frac{\partial \Psi^e}{\partial \mathbf{F}} \right) \left(\frac{\partial \mathbf{F}}{\partial \mathbf{u}} \right) d\xi \\ &= \chi^e V_e \mathbf{P}(\mathbf{F}) \left(\frac{\partial \mathbf{F}}{\partial \mathbf{u}} \right) = \chi^e \mathbf{f}_e^{int} \end{aligned} \quad (24)$$

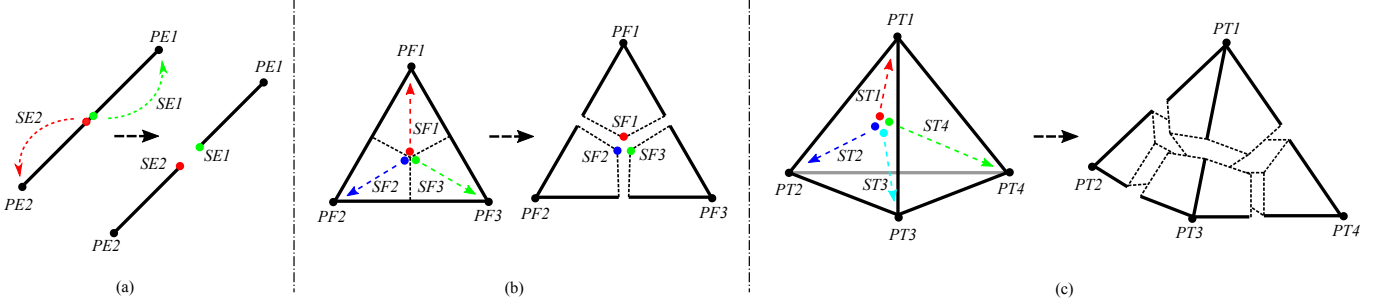


Fig. 6. Splitting of edge (left), face (middle) and tetrahedron (right) for visualization of fracture.

From the definition of the stiffness matrix for an individual element in Equation 10

$$\begin{aligned} \mathbf{k}_e^* &= \chi^e \int_{\Delta_e} \frac{\partial \mathbf{f}_e}{\partial \mathbf{u}} d\xi = \chi^e \int_{\Delta_e} \left(\frac{\partial \mathbf{f}_e}{\partial \mathbf{F}} \right) \left(\frac{\partial \mathbf{F}}{\partial \mathbf{u}} \right) d\xi \\ &= \chi^e V_e \left(\frac{\partial \mathbf{F}}{\partial \mathbf{u}} \right)^T \left(\frac{\partial \mathbf{P}}{\partial \mathbf{F}} \right) \left(\frac{\partial \mathbf{F}}{\partial \mathbf{u}} \right) = \chi^e \mathbf{k}_e \end{aligned} \quad (25)$$

Stiffness matrix of full system from equation 11,

$$\mathbf{K}^* = \sum_{e=1}^{n_{tet}} \chi^e \mathbf{k}_e \quad (26)$$

The mass matrix remains same as Equation 5 and the damping matrix takes the form of $\mathbf{b}_e^* = \alpha \mathbf{m}_e + \beta \mathbf{k}_e^* + \tilde{\mathbf{b}}_e$.

Plugging these updated parameters into Equation 4, we solve it for the complete fracture simulation. In order to implement our model for performing quasi-static simulations with no mass or damping matrix for regularization, we extend the code base released by [Smith et al. 2018]. For the complete dynamic simulation, we implement our model using the Vega FEM library [Sin et al. 2013].

4 VISUALIZATION OF FRACTURE

Our FEM computations are performed on the graph induced by the computational mesh, that is never remeshed. However, in order to visualize the fracture we need to split the mesh used for visualization. We clarify this distinction between the computational and visualization meshes using a simple 2D example. Figure 7b depicts that when a fracture occurs, the system dynamics is evaluated on the computational mesh with weakened elements. When we need to render the fractured elements, we split the mesh used for visualization, as shown in Figure 7c and reconstruct the fracture surface. The reconstruction of the fracture surface for visualization adds very little computational overhead to the overall simulation cost. We have already explained how the system dynamics is computed on the computational mesh in the presence of fracture.

We now explain the details of how we split the visualization mesh for rendering. We use a node associated four-split configuration of a tetrahedron, as shown in Figure 6c, for fracture visualization. When a tetrahedral element splits, the corresponding edges and faces of the element split too. As illustrated in Figure 6, in our current work we always split edges, faces and tetrahedra with respect to their centroids.

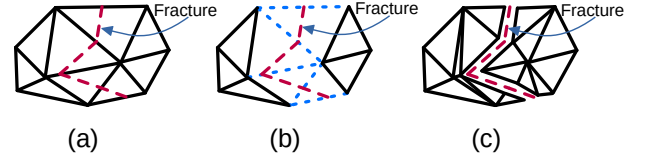


Fig. 7. (a) Original mesh with a fracture, (b) Computational mesh, with damaged edges marked in blue, on which system dynamics get evaluated, (c) Mesh for visualization is split and the fracture surface is reconstructed.

When normal stress along an edge, $PE1PE2$ (Figure 6a), crosses the critical threshold, it splits into two segments $PE1SE1$ and $PE2SE2$. $PE1$ and $PE2$ are original nodes in the mesh. Let us call them parent nodes. The other two newly generated nodes, $SE1$ and $SE2$, are called child nodes to $PE1$ and $PE2$, respectively. The child nodes do not contribute to the system dynamics but rather follow movements of their parent nodes. In a similar manner, when a face gets fractured into three segments (Figure 6b), three child nodes, $SF1$, $SF2$ and $SF3$ are assigned to their corresponding parent nodes, $PF1$, $PF2$ and $PF3$. Similarly four child nodes, $ST1$, $ST2$, $ST3$ and $ST4$ (Figure 6c) are assigned to four parent nodes $PT1$, $PT2$, $PT3$ and $PT4$ for a damaged tetrahedron. It is important to note that a triangular face or tetrahedron may not split into all three or four segments during the simulation. For example, with reference to Figure 6b, if we assume that only both the segments containing node $PF1$ get damaged i.e., edge $PE2PE3$ remains undamaged, then in such a case, child node $SF1$ follows the movement of parent node $PE1$ but child node $SF2$ and child node $SF3$ follow the average movement of parent nodes $PE2$ and $PE3$. When similar scenarios, although more complex, arise for a tetrahedron, we apply the same principle. All possible cases of different kinds of fracture are taken into account in our simulation.

5 RESULTS

We present multiple visualizations of fracture simulation for a variety of materials to demonstrate the robustness of our method and the diversity it can handle. We present quasi-static fracture simulation results first to exhibit the high stability achievable with our algorithm. Next we show dynamic fracture simulation results which mimic real world events like collision of hard objects with solid jade or glass objects and glass shells. We also show the effect of applying tensile or impact forces to rubber-like, and jello-like materials.

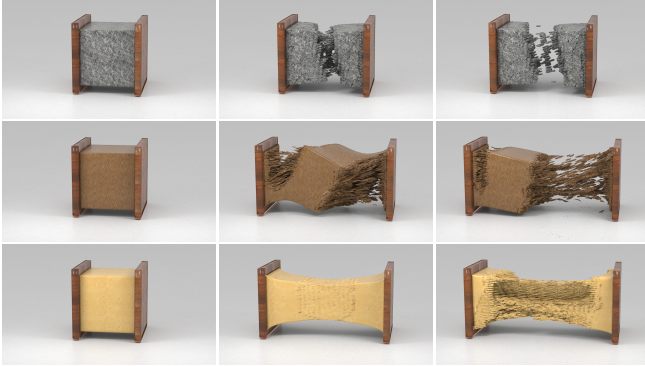


Fig. 8. Blocks made of different material are pulled apart in a quasi-static fracture simulation. We simulate blocks of stone (top row), soft Balsa wood (middle row) and cheese (bottom row).

Next, we experimentally validate our model by recreating a few benchmark fracture experiments in simulation that are commonly performed in a structural mechanics laboratory, with our framework and compare the results with expected results from similar experiments performed in the real world. These experimental simulations are complete dynamics simulations that demonstrate the accuracy of our method. Finally, we compare our method with existing related works.

For solving the system dynamics we use a regular Newton solver augmented with a line search [Smith et al. 2018] for quasi-static simulation and an implicit backward Euler integrator with a conjugate gradient solver [Sin et al. 2013] for dynamic simulation. All the simulations are performed on an Intel Core i7-9750H CPU with 12 threads at 2.60 GHz equipped with NVIDIA GeForce RTX 2060 graphics card. For visualization, the simulation results are raytraced in Houdini. Apart from the models obtained from the Stanford 3D scanning repository, the other 3D models used in this project are obtained from free3d.com and lifesciencedb.jp. Open-source software TetWild [Hu et al. 2018b] and TetGen [Si 2015] are used to generate the volumetric simulation meshes. Self-collision is not considered in our simulations. Mesh resolution and timing results for the simulations are reported in Table 2.

5.1 Quasi-Static Simulations

Here we use the stable Neo-Hookean energy defined in [Smith et al. 2018].

$$\Psi_{neo} = \frac{\mu}{2} (I_C - 3) + \frac{\lambda}{2} (J - \alpha) - \frac{\mu}{2} \log (I_C + 1) \quad (27)$$

where μ and λ are Lamé parameters and $\alpha = 1 + \frac{\mu}{\lambda} - \frac{\mu}{4\lambda}$.

Quasi-static experiments are performed in the absence of gravity, and mass & damping matrix regularizers. Using Equations 26, 1, 10 and 24, we can formulate the a quasi-static simulation as

$$\sum_{e=1}^{n_{tet}} \chi^e \mathbf{k}_e \mathbf{u} = \sum_{e=1}^{n_{tet}} \chi^e \mathbf{f}_e^{int} \quad (28)$$

First we take rectangular blocks of three materials: stone, soft Balsa wood and cheese whose points at both ends are fixed. Then we

<i>Simulation</i>	<i># Tetrahedra</i>	<i>sec/frame</i>
Stone (Fig. 8, 9)	168.2k	178.1
Soft Balsa wood (Fig. 8 9)	168.2k	189.6
Cheese (Fig. 8, 9)	168.2k	214.5
Loaf (Fig. 1)	620.6k	291.7
Jello armadillo (Fig. 2)	159.1k	78.9
Femur bone (Fig. 11)	21.6k	9.3
Solid glass armadillo (Fig. 18)	4.7k	2.1
Shell glass armadillo (Fig. 18)	41.1k	20.7
Solid tempered glass bunny (Fig. 19)	23.7k	11.8
Shell tempered glass bunny (Fig. 19)	38.8k	17.2
Rubber bunny (Fig. 12)	23.7k	10.9
NVE 36 steel bar (Fig. 13, 14)	27.8k	13.4
AWS 7018-G steel bar (Fig. 13, 14)	27.8k	13.1
Cement cylinder (Fig. 15)	45.8k	24.6

Table 2. Model resolution and the time taken per frame for all the simulations.



Fig. 9. Blocks made of different material are twisted in a quasi-static fracture simulation. We simulate blocks of stone (top row), soft Balsa wood (middle row) and cheese (bottom row).

pull each block from both ends by changing position of fixed points and examine the progressive fracture that results. This is shown in Figure 8 column wise, from left to right. Fracture of stone, soft Balsa wood and cheese are illustrated row wise from top to bottom. It can be seen from the figure that maximum diffusion of cracks is present in cheese and minimum in stone. We control the extent of crack diffusion in our method using different sizes of kernel support, R_d , (see Equation 20) for different material. Here e.g., we use $R_d = 0.0$ for stone, $R_d = 0.1$ for wood and $R_d = 0.5$ for cheese. This supports the claim that diffusion of cracks increase with increasing support of kernel. In Figure 9 we simulate the twisting of the same material blocks from both ends. While the stone block fractures instantly, the soft Balsa wood block breaks apart after much twisting. The

block made of even softer cheese like material does not break on twisting.

The quasi-static experiments not only exhibit the stability of our method but also give us a proper understanding about the effect of diffusion controlling parameter on fracture simulation. Along with Young's modulus and Poisson's ratio, this is also a very important tool for simulating fracture of different kinds of materials.

5.2 Dynamic Simulations

In a complete dynamic simulation we take into account the effects of external forces and solve full system dynamics as presented in Equation 2 with mass & damping matrix regularizers.

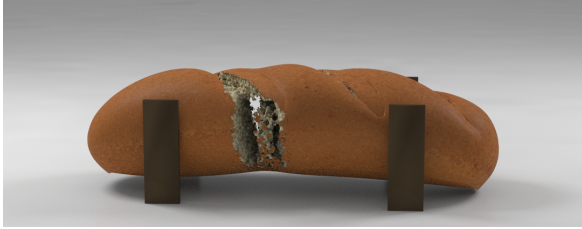


Fig. 10. Tearing a loaf of bread.

Here we use the invertible Saint–Venant Kirchhoff energy [Sin et al. 2013] defined as below.

$$\Psi_{stok} = \frac{\lambda}{8} (I_C - 3)^2 + \frac{\mu}{4} (II_C - 2I_C + 3) \quad (29)$$

where μ and λ are Lamé parameters. To begin with, in Figure 1 we



Fig. 11. Fracture of bone: splitting (left) and buckling (right).

illustrate the highly detailed and intricate fracture effects produced by tearing a loaf of bread. A frame from the same simulation is shown from another viewpoint in Figure 10. It is evident from these figures that our simulation model can model complex fracture patterns and can easily scale to high resolution meshes. In Figure 2 we simulate the limbs of a jello armadillo being ripped off. Here we also visualize the corresponding strain profiles. In the frame shown on the leftmost

side the armadillo appears just prior to fracture. Thus, it has highest strain at elements that are going to be damaged (coloured red). Once damage sets in post fracture, as shown on the right, the strain decreases again. The disconnected nodes in the damaged mesh have no strain value and thus appear in blue-green. In Figure 11, we show



Fig. 12. Deformation of a rubber bunny without any fracture.

frames from two simulations of fracture in a femur bone. Bone displays both brittle and quasi-ductile behavior depending on the direction of loading being applied [Peterlik et al. 2006]. The left image shows a simulation where we hold the bone at the bottom and apply a side impact force, thus causing a brittle, transverse split fracture [o AAOS 2020], caused by shear stresses that develop in the bone. On the right, we compress the bone, causing it to bend and behave in a quasi-ductile manner, producing a butterfly, comminuted or open fracture [o AAOS 2020]. This behavior of the bone emerges automatically from our simulation model.

In the top row of Figure 18, a solid ball hits an armadillo made of solid blue jade to generate large chunks of debris from the fracture. In the bottom row of the same figure, a solid ball smashes through a glass shell model of armadillo, leaving a hole in the model with associated debris.

When tempered glass, which is used in a car windscreen gets fractured it leaves a lot of spraying debris as if the glass has exploded. Using our fracture simulation method, in the top row of Figure 19 we render the fracture of a bunny made of solid tempered glass when it is hit by a solid ball. The fracture of a shell model of a bunny made of tempered glass is simulated in the bottom row of the same figure. Notice the intricate fracture pattern and spraying debris generated in both cases.

To depict that our method is capable of rendering proper deformation without any fracture, we simulate and visualize a ball hitting a rubber bunny in Figure 12. The model bends on impact, however, does not break.

5.3 Experimental Validation

In order to evaluate and validate how faithfully real world fracture can be simulated using our method, we present a qualitative and quantitative comparison with three benchmark laboratory fracture experiments. These are the Charpy impact test, the Izod impact test and the Brazilian test.

5.3.1 Charpy Impact Test. In this test we use a steel specimen of dimension $10mm \times 10mm \times 55mm$ with a 45° 'V' shaped groove in the middle of it (see left image of Figure 13). A pendulum of known mass and length then impacts the back of the groove with both ends of the specimen held against fixed beams. Now depending

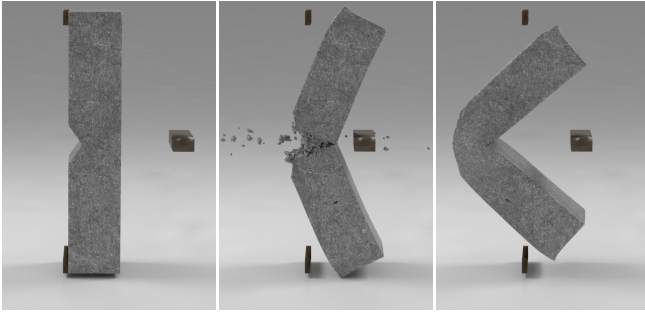


Fig. 13. **Charpy Impact Test:** The left image shows the configuration of the Charpy test. In the middle image a specimen with low tensile strength splits into two, while on the right a specimen with high tensile strength only bends and gets partially damaged.

on the tensile strength of the material, the specimen breaks fully into two pieces or is partially damaged and bends in a three point configuration. We simulate this experiment using our method, on specimens made of two different kinds of steel with different tensile strengths (the name of the steel is mentioned in Table 2). Instead of the entire swinging pendulum, as present in the real Charpy test setup, we simulate an impact with a fast moving block (as can be seen in the image) that hits the specimen at the same location where the specimen is supposed to be hit in the real test. As shown in Figure 13 the steel with lower tensile strength (middle image) breaks into two pieces while the other one (right image) splits partially and bends. Simulation material parameters used in this experiment are obtained from [Tronskar et al. 2002].

5.3.2 Izod Impact Test. The Izod impact test specimen is shown in the left image of Figure 14. Here the specimen is held in a cantilevered beam configuration with one end fixed and the pendulum hits it on the other end. The results of Izod test performed on the same materials as before, are shown in middle and right images of the figure.



Fig. 14. **Izod Impact Test:**The left image shows the configuration of the Izod test. In the middle image a specimen with low tensile strength splits into two, while on the right a specimen with high tensile strength only bends and gets partially damaged.

In Figure 16 we plot the load-displacement curves for the Charpy (middle) and Izod (right) tests respectively as obtained from our simulated experiments. The green curve denotes brittle fracture,

which splits sharply beyond a load threshold. Red curve which denotes ductile fracture, indicates a plastic flow in the material. The brittle and ductile fracture curves for both tests closely resemble the theoretical force-displacement curve shown on the left in the same figure [Tronskar et al. 2002]. Brittle material fractures completely after elastic region whereas ductile material partially fractures and then bends due to plasticity. This proves that brittle and ductile material simulation performed by our method closely matches the behaviour of real world materials, both qualitatively and quantitatively.

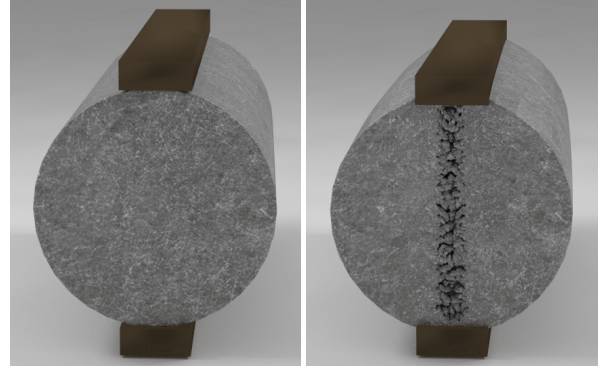


Fig. 15. **Brazilian test:** Initial (left) and fractured (right) configuration of cement cylinder.

5.3.3 Brazilian Test. The Brazilian test is a laboratory test for indirect measurement of tensile strength. In this test a vertical load is applied at the highest point of a cylinder, the axis of which is placed horizontally, and is supported on a horizontal plane. Here we use a cylinder of diameter 100mm and length 255mm made of ordinary portland cement. In Figure 15 the initial (left) and fractured (right) configuration of the cylinder are shown. We compare the precision of the experiment performed in simulation using our method with similar real experiment from literature [ExpeditionWorkshed 2013] by plotting their corresponding load displacement curves in Figure 17. The close match between the two curves validates the accuracy of our simulation model.

5.4 Comparison with Existing Techniques

To the best of our knowledge, this is the first work in computer graphics that presents a FEM-based fracture method that is graph-based, remeshing-free, highly stable and can incorporate large number of cracks with little extra computational overhead on FEM. Unlike XFEM [Chitalu et al. 2020] or VNA [Sifakis et al. 2007] [Wang et al. 2015], the size of system matrix remains constant throughout the simulation, thus reducing the computational cost over standard FEM substantially. While a state of the art XFEM-based fracture simulation [Chitalu et al. 2020] requires 1539 sec to render a single frame for a 40k model, our model requires 291.7 sec to render a frame for the simulation of an extremely complex loaf model consisting of 620.6k tetrahedra. Moreover, simulating spraying debris like fracture of tempered glass with existing FEM or XFEM based solutions in literature will require prohibitively expensive numerical

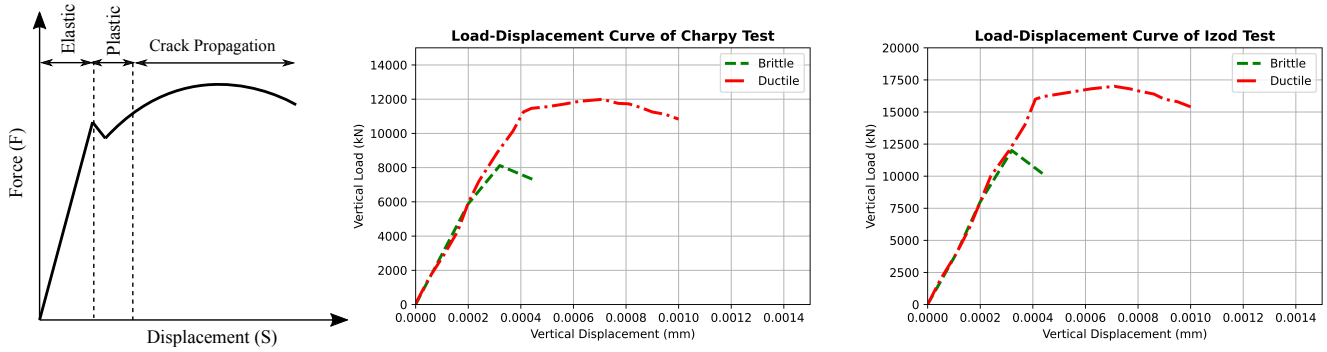


Fig. 16. The left plot shows the theoretically expected force-displacement curve for the fracture of a material. The center and the right plots show the load-displacement curve of our simulated Charpy and Izod impact tests respectively.

Comparison Table

Method	R.F.	R.C.S.	E.E.B.	C.C.	R.D.B.	Stability
FEM [O'Brien et al. 2002] [Koschier et al. 2015] [Pfaff et al. 2014]	No	No	Easy	High	Yes	High
XFEM [Chitalu et al. 2020]	Yes	Yes	Easy	High	No	Low
VNA [Sifakis et al. 2007] [Wang et al. 2015]	Yes	Yes	Easy	High	Yes	Low
BEM [Hahn and Wojtan 2015] [Hahn and Wojtan 2016]	No	No	Easy	Very High	No	High
Peridynamics [Chen et al. 2018] [Levine et al. 2015]	Yes	No	Easy	Very High	Yes	Low
MPM [Wolper et al. 2019] [Wolper et al. 2020]	Yes	No	Difficult	Medium	Yes	High
Our method	Yes	No	Easy	Very Low	Yes	Very High

Table 3. Comparison with existing frameworks. R.F., R.C.S., E.E.B., C.C. and R.D.B. denote Remeshing-Free, Require Changing the Initial System matrix, Enforcing Essential Boundary conditions, Computational Cost and Render both Ductile and Brittle Fracture respectively.

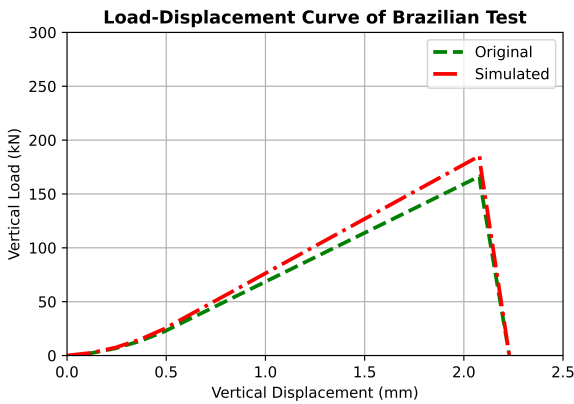


Fig. 17. **Brazilian test:** Load displacement curve for original and simulated experiments.

computation due to remeshing and rapid scaling of the system matrix. Our method can simulate a very high amount of fracture debris easily. Our method enjoys the good characteristics of both FEM and XFEM methods, without the overheads. Additionally, it does not suffer from the limitations of MPM and BEM based methods such as difficulty in enforcing essential boundary conditions, poor performance in rendering fracture of rigid objects, rigidity of fragmented

elements and expensive computation. A feature based comparison of our model over other existing frameworks is presented in Table 3.

6 CONCLUSION

We present a novel graph-based FEM based remeshing-free approach for ductile and brittle fracture. The high stability, speed and robustness of our method is illustrated and established via both quasi-static and dynamic experiments. We evaluate the appeal and realism of our fracture simulations through results on objects made of a wide variety of materials. Comparing with benchmark fracture experiments, we validate the correctness and accuracy of our method.

6.1 Limitations and Future Work

Even though we believe that our method is capable of producing particularly realistic fracture of a variety of materials at a high speed, it does have some limitations in its current form. We have not explored anisotropic fracture exhaustively. Also, currently an edge of an element in the object mesh can split in maximum two parts, thus limiting the fracture of tetrahedral elements at maximum to four parts. We wish to extend our work to incorporate high number of fracture segments in a single element.

Finally, in our current implementation we do not model plasticity explicitly. But we notice that many tetrahedral elements in the mesh do not completely split into two or more distinct segments



Fig. 18. Fracture of an armadillo model made of solid blue jade (top row) and glass shell (bottom row).

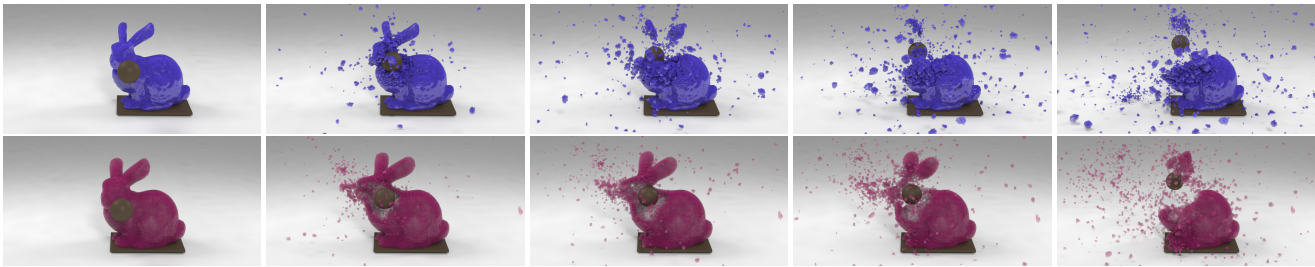


Fig. 19. Fracture of a bunny model made of solid tempered glass (top row) and a tempered glass shell (bottom row).

but contain damaged edges. These damaged elements with lower elastic strain energy fail to restore to their rest configuration, which implicitly produces a plasticity like effect in the object. We wish to develop a complete plasticity solution suitable for our graph-based FEM in future work.

REFERENCES

- K. Aoki, N. H. Dong, T. Kaneko, and S. Kuriyama. 2004. Physically based simulation of cracks on drying 3D solids. In *Proceedings Computer Graphics International, 2004*. IEEE, 357–364.
- Zhaosheng Bao, Jeong-Mo Hong, Joseph Teran, and Ronald Fedkiw. 2007. Fracturing Rigid Materials. *IEEE Transactions on Visualization and Computer Graphics* 13, 2 (March 2007), 370–378. <https://doi.org/10.1109/TVCG.2007.39>
- Adam W. Bargteil, Chris Wojtan, Jessica K. Hodgins, and Greg Turk. 2007. A Finite Element Method for Animating Large Viscoplastic Flow. *ACM Trans. Graph.* 26, 3 (July 2007), 16–es. <https://doi.org/10.1145/1276377.1276397>
- Wei Chen, Fei Zhu, Jing Zhao, Sheng Li, and Guoping Wang. 2018. Peridynamics-Based Fracture Animation for Elastoplastic Solids. *Computer Graphics Forum* 37, 1 (2018), 112–124. <https://doi.org/10.1111/cgf.13236> arXiv:<https://onlinelibrary.wiley.com/doi/pdf/10.1111/cgf.13236>
- Zhili Chen, Miaojun Yao, Renguo Feng, and Huamin Wang. 2014. Physics-Inspired Adaptive Fracture Refinement. *ACM Trans. Graph.* 33, 4, Article 113 (July 2014), 7 pages. <https://doi.org/10.1145/2601097.2601115>
- Floyd M. Chitalu, Qinghai Miao, Kartic Subr, and Taku Komura. 2020. Displacement-Correlated XFEM for Simulating Brittle Fracture. *Computer Graphics Forum* 39, 2 (2020), 569–583. <https://doi.org/10.1111/cgf.13953> arXiv:<https://onlinelibrary.wiley.com/doi/pdf/10.1111/cgf.13953>
- ExpeditionWorkshed. 2013. Brazilian Test - Tensile Failure of Concrete in Slow Motion. Retrieved September 2, 2020 from https://www.youtube.com/watch?v=6lkZrLp_mE
- David Hahn and Chris Wojtan. 2015. High-Resolution Brittle Fracture Simulation with Boundary Elements. *ACM Trans. Graph.* 34, 4, Article 151 (July 2015), 12 pages. <https://doi.org/10.1145/2766896>
- David Hahn and Chris Wojtan. 2016. Fast Approximations for Boundary Element Based Brittle Fracture Simulation. *ACM Trans. Graph.* 35, 4, Article 104 (July 2016), 11 pages. <https://doi.org/10.1145/2897824.2925902>
- Koichi Hirota, Yasuyuki Tanoue, and Toyohisa Kaneko. 1998. Generation of crack patterns with a physical model. *The Visual Computer* 14 (1998), 126 – 137. <https://doi.org/10.1007/s003710050128>
- Koichi Hirota, Yasuyuki Tanoue, and Toyohisa Kaneko. 2000. Simulation of three-dimensional cracks. *The Visual Computer* 16 (2000), 371 – 378. <https://doi.org/10.1007/s003710000069>
- Yuanming Hu, Yu Fang, Ziheng Ge, Ziyin Qu, Yixin Zhu, Andre Pradhana, and Chenfanfu Jiang. 2018a. A Moving Least Squares Material Point Method with Displacement Discontinuity and Two-Way Rigid Body Coupling. *ACM Trans. Graph.* 37, 4, Article 150 (July 2018), 14 pages. <https://doi.org/10.1145/3197517.3201293>
- Yixin Hu, Qingnan Zhou, Xifeng Gao, Alec Jacobson, Denis Zorin, and Daniele Panozzo. 2018b. Tetrahedral Meshing in the Wild. *ACM Trans. Graph.* 37, 4, Article 60 (July 2018), 14 pages. <https://doi.org/10.1145/3197517.3201353>
- Doug L. James and Dinesh K. Pai. 1999. ArtDefo: Accurate Real Time Deformable Objects. In *Proceedings of the 26th Annual Conference on Computer Graphics and Interactive Techniques (SIGGRAPH '99)*. ACM Press/Addison-Wesley Publishing Co., USA, 65–72. <https://doi.org/10.1145/311535.311542>
- Chenfanfu Jiang, Craig Schroeder, Joseph Teran, Alexey Stomakhin, and Andrew Selle. 2016. The Material Point Method for Simulating Continuum Materials. In *ACM SIGGRAPH 2016 Courses (SIGGRAPH '16)*. Association for Computing Machinery, New York, NY, USA, Article 24, 52 pages. <https://doi.org/10.1145/2897826.2927348>
- Parisa Khodabakhshi, J. N. Reddy, and Arun Srinivasa. 2016. GraFEA: a graph-based finite element approach for the study of damage and fracture in brittle materials. *Meccanica* 51 (2016), 3129 – 3147. <https://doi.org/10.1007/s11012-016-0560-6>

- Parisa Khodabakhshi, J. N. Reddy, and Arun Srinivasa. 2019. A nonlocal fracture criterion and its effect on the mesh dependency of GraFEA. *Acta Mechanica* 230 (2019), 3593–3612. <https://doi.org/10.1007/s00707-019-02479-8>
- Dan Koschier, Jan Bender, and Nils Thuerey. 2017. Robust Extended Finite Elements for Complex Cutting of Deformables. *ACM Trans. Graph.* 36, 4, Article 55 (July 2017), 13 pages. <https://doi.org/10.1145/3072959.3073666>
- Dan Koschier, Sebastian Lippner, and Jan Bender. 2015. Adaptive Tetrahedral Meshes for Brittle Fracture Simulation. In *Proceedings of the ACM SIGGRAPH/Eurographics Symposium on Computer Animation (SCA '14)*. Eurographics Association, Goslar, DEU, 57–66.
- J. A. Levine, A. W. Bargteil, C. Corsi, J. Tessendorf, and R. Geist. 2015. A Peridynamic Perspective on Spring-Mass Fracture. In *Proceedings of the ACM SIGGRAPH/Eurographics Symposium on Computer Animation (SCA '14)*. Eurographics Association, Goslar, DEU, 47–55.
- Neil Molino, Zhaosheng Bao, and Ron Fedkiw. 2004. A Virtual Node Algorithm for Changing Mesh Topology during Simulation. In *ACM SIGGRAPH 2004 Papers (SIGGRAPH '04)*. Association for Computing Machinery, New York, NY, USA, 385–392. <https://doi.org/10.1145/1186562.1015734>
- Matthias Müller and Markus Gross. 2004. Interactive Virtual Materials. In *Proceedings of Graphics Interface*. Canadian Human-Computer Communications Society, Waterloo, CAN, 239–246.
- Alan Norton, Greg Turk, Bob Bacon, John Gerth, and Paula Sweeney. 1991. Animation of fracture by physical modeling. *The Visual Computer* 7 (1991), 210–219. <https://doi.org/10.1007/BF01900837>
- OrthoInf o AAOS. 2020. Femur Shaft Fractures (Broken Thighbone). Retrieved December 30, 2020 from <https://orthoinfo.aaos.org/en/diseases--conditions/femur-shaft-fractures-broken-thighbone/>
- James F. O'Brien, Adam W. Bargteil, and Jessica K. Hodgins. 2002. Graphical Modeling and Animation of Ductile Fracture. *ACM Trans. Graph.* 21, 3 (July 2002), 291–294. <https://doi.org/10.1145/566654.566579>
- James F. O'Brien and Jessica K. Hodgins. 1999. Graphical Modeling and Animation of Brittle Fracture. In *Proceedings of the 26th Annual Conference on Computer Graphics and Interactive Techniques (SIGGRAPH '99)*. ACM Press/Addison-Wesley Publishing Co., USA, 137–146. <https://doi.org/10.1145/311535.311550>
- Mark Pauly, Richard Keiser, Bart Adams, Philip Dutré, Markus Gross, and Leonidas J. Guibas. 2005. Meshless Animation of Fracturing Solids. In *ACM SIGGRAPH 2005 Papers (SIGGRAPH '05)*. Association for Computing Machinery, New York, NY, USA, 957–964. <https://doi.org/10.1145/1186822.1073296>
- Herwig Peterlik, Paul Roschger, Klaus Klaushofer, and Peter Fratzl. 2006. From brittle to ductile fracture of bone. *Nature materials* 5, 1 (2006), 52–55.
- Tobias Pfaff, Rahul Narain, Juan Miguel de Joya, and James F. O'Brien. 2014. Adaptive Tearing and Cracking of Thin Sheets. *ACM Trans. Graph.* 33, 4, Article 110 (July 2014), 9 pages. <https://doi.org/10.1145/2601097.2601132>
- J.N. Reddy and Arun Srinivasa. 2015. On the force–displacement characteristics of finite elements for elasticity and related problems. *Finite Elements in Analysis and Design* 104 (2015), 35–40. <https://doi.org/10.1016/j.finel.2015.04.011>
- Hang Si. 2015. TetGen, a Delaunay-Based Quality Tetrahedral Mesh Generator. *ACM Transactions on Mathematical Software (TOMS)* 41, 2, Article 11 (Feb. 2015), 36 pages. <https://doi.org/10.1145/2629697>
- Eftychios Sifakis and Jernej Barbic. 2012. FEM Simulation of 3D Deformable Solids: A Practitioner's Guide to Theory, Discretization and Model Reduction. In *ACM SIGGRAPH 2012 Courses (SIGGRAPH '12)*. Association for Computing Machinery, New York, NY, USA, Article 20, 50 pages. <https://doi.org/10.1145/2343483.2343501>
- Eftychios Sifakis, Kevin G. Der, and Ronald Fedkiw. 2007. Arbitrary Cutting of Deformable Tetrahedralized Objects. In *Proceedings of the 2007 ACM SIGGRAPH/Eurographics Symposium on Computer Animation (SCA '07)*. Eurographics Association, Goslar, DEU, 73–80.
- F. S. Sin, D. Schroeder, and J. Barbic. 2013. Vega: Non-Linear FEM Deformable Object Simulator. *Computer Graphics Forum* 32, 1 (2013), 36–48. <https://doi.org/10.1111/j.1467-8659.2012.03230.x> arXiv:<https://onlinelibrary.wiley.com/doi/pdf/10.1111/j.1467-8659.2012.03230.x>
- Breannan Smith, Fernando De Goes, and Theodore Kim. 2018. Stable Neo-Hookean Flesh Simulation. *ACM Trans. Graph.* 37, 2, Article 12 (March 2018), 15 pages. <https://doi.org/10.1145/3180491>
- Alexey Stomakhin, Craig Schroeder, Lawrence Chai, Joseph Teran, and Andrew Selle. 2013. A Material Point Method for Snow Simulation. *ACM Trans. Graph.* 32, 4, Article 102 (July 2013), 10 pages. <https://doi.org/10.1145/2461912.2461948>
- Demetri Terzopoulos and Kurt Fleischer. 1988. Modeling Inelastic Deformation: Viscoelasticity, Plasticity, Fracture. *SIGGRAPH Comput. Graph.* 22, 4 (June 1988), 269–278. <https://doi.org/10.1145/378456.378522>
- J.P. Tronkar, M.A. Mannan, and M.O. Lai. 2002. Measurement of fracture initiation toughness and crack resistance in instrumented Charpy impact testing. *Engineering Fracture Mechanics* 69, 3 (2002), 321–338. [https://doi.org/10.1016/S0013-7944\(01\)00077-7](https://doi.org/10.1016/S0013-7944(01)00077-7)
- Stephanie Wang, Mengyuan Ding, Theodore F. Gast, Leyi Zhu, Steven Gagniere, Chenfanfu Jiang, and Joseph M. Teran. 2019. Simulation and Visualization of Ductile Fracture with the Material Point Method. *Proc. ACM Comput. Graph. Interact. Tech.* 2, 2, Article 18 (July 2019), 20 pages. <https://doi.org/10.1145/3340259>
- Yuting Wang, Chenfanfu Jiang, Craig Schroeder, and Joseph Teran. 2015. An Adaptive Virtual Node Algorithm with Robust Mesh Cutting. In *Proceedings of the ACM SIGGRAPH/Eurographics Symposium on Computer Animation (SCA '14)*. Eurographics Association, Goslar, DEU, 77–85.
- Martin Wicke, Daniel Ritchie, Bryan M. Klingner, Sebastian Burke, Jonathan R. Shewchuk, and James F. O'Brien. 2010. Dynamic Local Remeshing for Elastoplastic Simulation. In *ACM SIGGRAPH 2010 Papers (SIGGRAPH '10)*. Association for Computing Machinery, New York, NY, USA, Article 49, 11 pages. <https://doi.org/10.1145/1833349.1778786>
- Joshua Wolper, Yunuo Chen, Minchen Li, Yu Fang, Ziyin Qu, Jiecong Lu, Meggie Cheng, and Chenfanfu Jiang. 2020. AnisoMPM: Animating Anisotropic Damage Mechanics. *ACM Trans. Graph.* 39, 4, Article 37 (July 2020), 16 pages. <https://doi.org/10.1145/3386569.3392428>
- Joshua Wolper, Yu Fang, Minchen Li, Jiecong Lu, Ming Gao, and Chenfanfu Jiang. 2019. CD-MPM: Continuum Damage Material Point Methods for Dynamic Fracture Animation. *ACM Trans. Graph.* 38, 4, Article 119 (July 2019), 15 pages. <https://doi.org/10.1145/3306346.3322949>
- Hongyi Xu, Funshing Sin, Yufeng Zhu, and Jernej Barbic. 2015. Nonlinear Material Design Using Principal Stretches. *ACM Trans. Graph.* 34, 4, Article 75 (July 2015), 11 pages. <https://doi.org/10.1145/2766917>
- Yufeng Zhu, Robert Bridson, and Chen Greif. 2015. Simulating Rigid Body Fracture with Surface Meshes. *ACM Trans. Graph.* 34, 4, Article 150 (July 2015), 11 pages. <https://doi.org/10.1145/2766942>